FINITE ELEMENT STUDIES OF COLLOIDAL MIXTURES INFLUENCED BY

ELECTRIC FIELDS

A Thesis

by

FRANKLIN JERREL DRUMMOND

Submitted to the Office of Graduate Studies of
Texas A&M University
in partial fulfillment of the requirements for the degree of

MASTER OF SCIENCE

August 2011

Major Subject: Aerospace Engineering

FINITE ELEMENT STUDIES OF COLLOIDAL MIXTURES INFLUENCED BY

ELECTRIC FIELDS

A Thesis

by

FRANKLIN JERREL DRUMMOND

Submitted to the Office of Graduate Studies of
Texas A&M University
in partial fulfillment of the requirements for the degree of

MASTER OF SCIENCE

Approved by:

Chair of Committee,	James G. Boyd IV
Committee Members,	Gregory H. Huff
	John D. Whitcomb
Head of Department,	Dimitris Lagoudas

August 2011

Major Subject: Aerospace Engineering

ABSTRACT

Finite Element Studies of Colloidal Mixtures Influenced by

Electric Fields. (August 2011)

Franklin Jerrel Drummond, B.S., Texas A&M University

Chair of Advisory Committee: Dr. James G. Boyd IV

A further understanding of colloidal mixture behavior under applied electric fields would greatly benefit the design of smart material systems such as electrorheological fluidic devices and microfluidic reconfigurable antennas. This thesis presents a finite element analysis of colloidal mixture electrokinetic behavior. Computations of particle forces as a function of applied frequency and particle shape were performed. An effective medium property method was also studied.

Fluidic and electric forces were obtained with various applied excitation frequencies throughout three locations in a coplanar microelectrode domain. This domain consists of two 50 nm thick gold electrodes separated by a 30 μm gap. The three locations are 1.2 μm, 40 μm, and 90 μm from the gap center. Total force vectors were computed by integrating Maxwell and Cauchy stress tensors to determine whether the particles are pushed toward or away from the electrode gap at frequencies of 10 Hz, 1 kHz, and 100 kHz. It was determined that particles were pushed outside the gap at median frequencies of 1kHz (indicating ac electroosmotic force domination) and began to be pushed back

toward the gap at higher frequencies of 100 kHz (indicating dielectrophoretic force intensification).

Particle shape effects were examined by calculating the electrical interparticle force between two particles at various incidences with respect to a uniform electric field. Particle attraction occurs when the line between the particle centers is aligned with the electric field; repulsion occurs when this center line is perpendicular. The incidence angle at which the particles switch from attraction to repulsion is defined as θ_{cr}. The aspect ratio and particle edge separation distances used in this study were 1, 5,12.92 and 0.25 µm, 0.50 µm, 2.0 µm, respectively. The results indicate that higher aspect ratio particles tend to have smaller θ_{cr} values and larger interparticle force magnitudes for given separation distances.

Finally, effective dielectric constant simulations utilizing periodic crystalline arrangements of colloidal structure were performed. The results show good agreement with the Maxwell Garnett mixing rule at volume fractions above 30%. Less canonical structures of cubic particles were also modeled.

ACKNOWLEDGEMENTS

I would like to thank my thesis advisor, Dr. James Boyd, for providing guidance in developing this thesis and the research presented herein. I would also like to thank the other members of my committee, Dr. Gregory Huff and Dr. Whitcomb. Dr. Huff helped me develop these ideas more coherently, and Dr. Whitcomb helped me fill my committee out on short notice.

I would also like to thank all my fellow graduate students, in both the aerospace and electrical engineering departments. They helped me out with some of the finer points of grammatical and formatting issues. It was very nice to have a set of people to bounce my ideas off of and this helped tremendously.

I could not have finished this work without the love and support from my family, including my parents and brother. They provided great love and encouragement throughout the development of this work.

Finally, I would like to thank my Lord and Savior, Jesus Christ. Through Him, I have been given the strength and motivation to complete this work, and all glory belongs to Him.

TABLE OF CONTENTS

LIST OF FIGURES

FIGURE   Page

LIST OF TABLES

CHAPTER I

INTRODUCTION

Colloidal dispersions are used in many important technologies. Two examples of this are in electrorheological fluids (ERFs) and electrically tunable circuits and antennas [1-2]. A colloidal dispersion (for the purposes in this thesis) consists of nanoparticles dispersed into a fluidic medium. Different particle configurations and distributions can be achieved by applying various electric fields to these dispersions. These different particle distributions can yield vastly different aggregate electrical and mechanical properties. For example, in electrorheological fluids the viscosity can be adjusted up to five orders of magnitude through the application of an electric field. This phenomenon is being analyzed and applied for use in various smart braking and suspension technologies. An example of this in Fig. 1 shows an ERF material being used to modulate the resistance of a braking mechanism for leg extension exercises [3].

This design was proposed for isotonic and isokinetic exercises typically used in a knee rehabilitation program. It operates by adjusting the electric field applied to the ERF material (located in the disc region at the knee joint). The ERF viscosity increases upon application of an electric field (and vice versa) and thereby increases the resistance in the knee joint to assist in motion control.

_____

This thesis follows the style of *IEEE Transactions on Antennas and Propagation*.
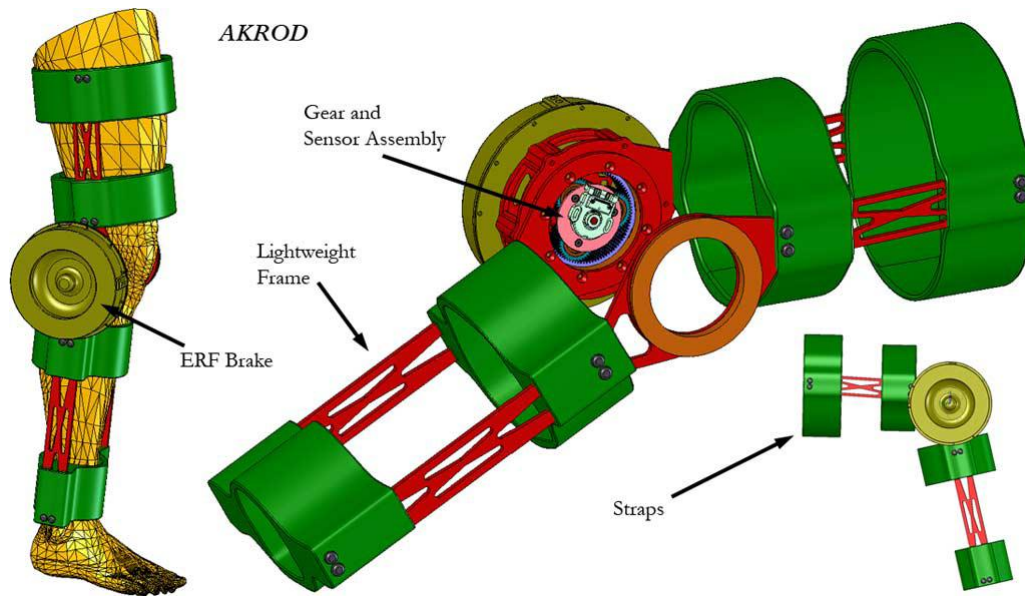
Fig. 1. Active knee rehabilitation device using an ERF [3]

Fig. 2 shows a more relevant example of a device using the electrokinetic behavior of nanoparticles dispersed in a fluidic medium [4]. Electric potential applied across the electrodes acts a switching mechanism from the "OFF" position to the "ON" position, where the colloidal dispersion in the "ON" position has a higher conductivity across the gap and net viscosity than that of the "OFF" position. If these were dielectric particles, this same configuration would have raised the effective dielectric constant across the gap. This will be discussed in more detail in Chapter III. ***This thesis will evaluate this type of electrokinetic behavior using finite element simulations to predict a) the dominant forces on the particles and b) the impact of particle aspect ratio on these forces.***

Fig. 2. "Off" and "On" particle distributions [4]

Colloidal dispersions can also be used in very different applications. For example, the dielectric constant within circuits and antenna structures can be strategically tuned by changing the nanoparticle distribution, concentration, and composition. Fig. 3 shows two antenna-based applications which use this type of tuning to enable reconfiguration [4-5]. The microstrip patch antenna (left side of Fig. 3) has capillaries embedded into its substrate in which the fluidic dispersions can be manipulated [5]. The antenna's resonant frequency can be changed by varying the dielectric constant of these materials (through mixing, etc.). Barium Strontium Titanate (BSTO) nanoparticles are dispersed in silicone oil and used as the colloidal dispersion in this application. Operationally speaking, this creates an increase in the dispersion's dielectric constant that causes an extension of effective electrical length. This in turn causes a decrease in the resonant frequency and the operational impedance bandwidth; these are two metrics which can be used to characterize the antenna's operation.

The right side of Fig. 3 shows another example of a reconfigurable antenna enabled by dispersions [4]. This cross dipole consists of a patch antenna structure with four copper

patches surrounding an electrically-fed central patch. Fig. 4 shows the circuit model for this antenna [4]. Placing a high dielectric colloidal material in the gap region increases the gap capacitance and decreases the gap impedance so surface currents can cross from the central patch to an outer patch. These surface currents create radiation polarized in the current direction. For example, polarization in the horizontal direction (as shown in Fig. 3) can be achieved by placing a high dielectric material in gaps 1 and 3. The design and analysis of these reconfigurable antennas necessitates understanding of the effective medium colloidal dielectric constant. ***This thesis will compare finite element simulations to analytical mixing formulas for canonical particle geometries and then use these numerical methods predict the effective medium properties of dispersions using non-canonical particle topologies without analytical solutions.***
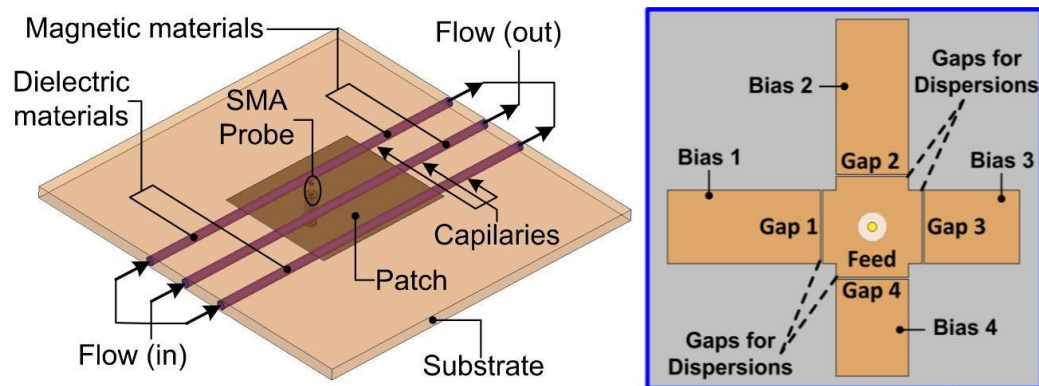
Fig. 3. Frequency (left) and polarization (right) reconfigurable antennas [4-5]
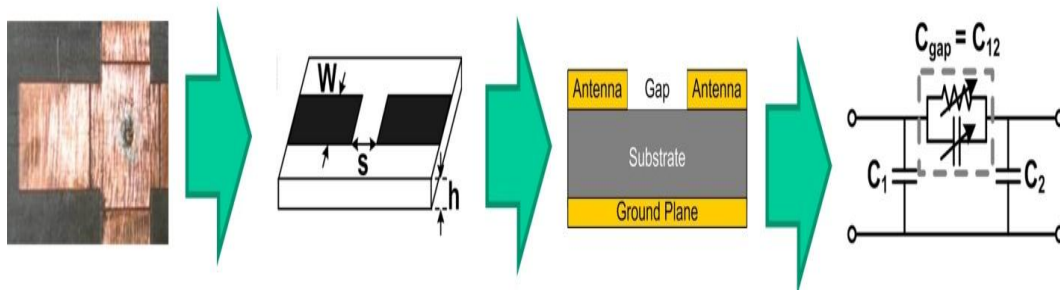
Fig. 4. Circuit model of polarization reconfigurable antenna [4]

Both the ERF devices and the polarization reconfigurable antenna apply electric fields to the dispersion to achieve a certain material property. There are many control variables for the design of these systems including:

- Excitation voltage amplitude

- Excitation frequency

- Electrode distribution

- Electrode shape

- Particle size

- Particle shape (i.e. spherical, whiskers, etc.)

- Medium and particle electrical properties

Better devices can be designed when the effects of each of these control variables on the colloidal dispersion dielectric constant is understood. This thesis will study the effects of particle shape and excitation frequency.

This thesis presents a series of three colloidal particle finite element studies that provide key insight into the aforementioned device design. The approach can best be seen by examining Fig. 5. The design of the material aspects of these devices involves finding the right processing conditions (control variables discussed above) to achieve a microstructure that yields the desired effective properties. Chapters III and IV examine the effects of frequency and particle shape on the forces applied to the colloidal particles. The dominant forces indicate key characteristics of the resultant microstructure. Dielectrophoretic force domination will produce particle chain formation while AC electroosmotic force domination will produce particles ejected from the electrode gap. Chapter V uses a finite element periodic method to find the homogenized dielectric constant based on particle distribution. This method is first verified against a classical mixing rule. A complex particulate system involving cubic particles is then analyzed.
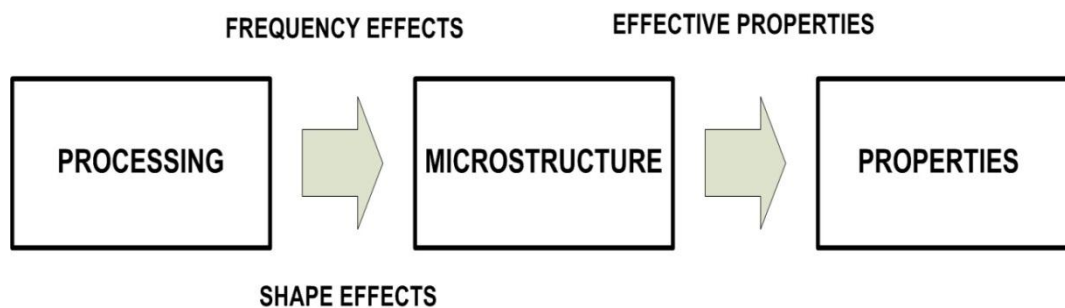
Fig. 5. Thesis approach

All simulations were performed with COMSOL, a commercial multiphysics finite element partial differential equation solver. This program was chosen based on its ease in coupling various physics together such as the electric and fluidic phenomena. This

feature is especially useful in the area of colloidal mixtures due to the many types of physics involved.

The first study shown in Chapter III seeks to validate the interpretation of the frequency-dependent experimental results by Bahukudumbi *et al*. [6]. These experiments involved 800 nm gold colloids in electrolytic water with fields applied by two coplanar parallel electrodes. The resulting colloidal microstructure was shown to be heavily frequency-dependent. These experimental results were first interpreted in terms of a competition between three electrokinetic phenomena: electrophoresis, AC electroosmosis, and dielectrophoresis [7]. Dielectrophoretic and AC electroosmotic forces were computed at the experimental frequencies to observe if total force magnitudes and directions agreed with the experimental results. Identifying the key forces involved at each frequency regime makes it possible to determine the particle configuration; and hence, the effective dielectric constant.

The second study shown in Chapter IV examines the effects of shape on particle attraction. The interparticle force between two TiO_2 particles in a uniform unidirectional electric field was calculated. The particle aspect ratio, separation distance, and separation angle with respect to the field orientation were varied as the interparticle force was calculated by integrating the Maxwell stress tensor. Then interparticle force vs. incidence angle relationships were compared between different aspect ratios and

separation distances. This analysis yields information about the particle regions of attraction and force magnitudes as a function of aspect ratio.

The third study shown in Chapter V consists of an effective dielectric constant finite element analysis of BSTO particles in silicone oil. This analysis was performed for various particle configurations and volume fractions. These configurations consisted of simple-cubic and face-centered cubic (FCC) lattices. The effective properties were calculated using techniques illustrated in Lee *et al.* [8]. These resultant effective properties were then compared with the Maxwell Garnett mixing rule, a well-known and established formula for computing effective properties [9]. Less canonical structures of cubic particles were analyzed after comparison of simpler particle geometry results with the Maxwell Garnett mixing rule.

CHAPTER II

BACKGROUND

The goal of this chapter is to provide technical background and evaluate the numerical accuracy of COMSOL by investigating several canonical structures with well-known analytical solutions. The polarization phenomenon will first be discussed along with the field perturbation effects due to dielectric constant contrast between a particle and surrounding medium. The quasi-static charge conservation formulation will be presented next for the frequency-dependent problem to be discussed in Chapter III. The methods for calculating the electrical and fluid forces will then be presented. Finally, test problems that were used to validate the finite element force calculations will be discussed.

A. Polarization and Effects of Dielectric Constant Contrast

Gauss's Law for free space can be expressed as (1).

$$\nabla \bullet \vec{E} = \frac{\rho}{\varepsilon_0} \tag{1}$$

Fig. 6 presents the polarization of a dielectric particle in a uniform electric field. When the field, E_{ext}, is applied, an internal separation of charges in the particle occurs which creates a small electric field, E_p, that is antiparallel to the external field. This field-induced polarization creates a smaller electric field inside the particle due to the superposition of E_p and E_{ext}.
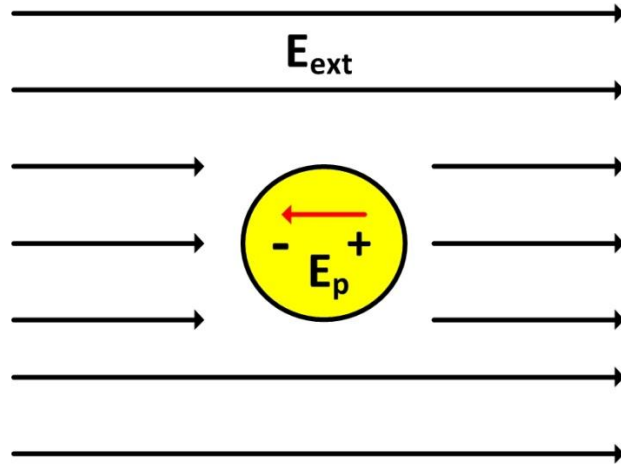
Fig. 6. Polarization of particle in uniform electric field

The field induced polarization can be modeled according to (2).

$$\vec{E}_p = \varepsilon_0 \vec{E} \chi_e \tag{2}$$

Substituting (2) into (1) and applying the superposition of fields results in (3).

$$\nabla \bullet \left[\varepsilon_0 \vec{E} (1 - \chi_e) \right] = \rho \tag{3}$$

The dielectric constant and electric displacement are defined as (4) and (5), respectively.

$$\varepsilon = \varepsilon_0 (1 - \chi_e) \tag{4}$$

$$\vec{D} = \varepsilon \vec{E} \tag{5}$$

Combining (4),(5) and (3) results in Gauss's law for a dielectric material which is shown in (6).

$$\nabla \bullet \left(\vec{D} \right) = \rho \tag{6}$$

The effect of dielectric contrast between the particle and the medium will now be analyzed. Figs. 7 and 8 display the field perturbation caused by two particles in uniform electric field. In Fig. 7, the particle has a dielectric constant smaller than that of the

medium by a factor of 1000. In Fig. 8, the medium has a dielectric constant greater than that of the medium by a factor of 1000.
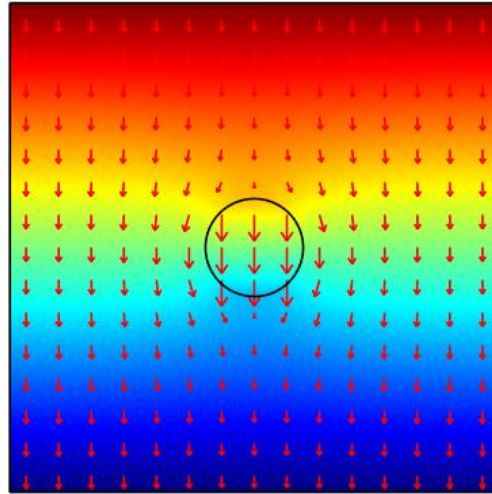
Fig. 7. Electric field for lower particle dielectric constant
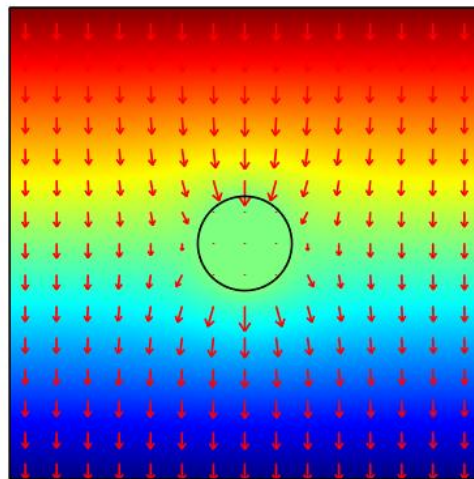
Fig. 8. Electric field for higher particle dielectric constant

Notice that in Fig. 7, the field inside the particle is greater than the external field, and in Fig. 8, the internal field is weaker than the external field. This analysis demonstrates that higher dielectric constant regions will have lower field intensities for the electrostatic case with no sources. This is consistent with the analysis above since higher dielectric constant regions will have a higher induced field which is antiparallel to the external field. This induced field weakens the overall field inside the particle.

B. Quasi-static Definition and Charge Conservation Formulation

The frequency-dependence study was modeled using the quasi-static approximation. It is assumed that all currents and charges vary so slowly in time that the sources can be assumed to be stationary under the quasi-static approximation [10]. This approximation is valid when the electrical size defined as the ratio between the wavelength, λ, and the characteristic dimension, L, is smaller than 10^{-1}. Under this approximation, Maxwell's differential equations involving the electric field reduce to (7) and (8).

$$\nabla \bullet \left(\vec{D} \right) = \rho \tag{7}$$

$$\nabla \times \vec{E} = 0 \tag{8}$$

For a linear dielectric, the constitutive relation between the electric displacement and the field can be expressed as (9).

$$\vec{D} = \varepsilon \vec{E} \tag{9}$$

Substituting (9) into (7) gives (10).

$$\nabla \bullet \left(\varepsilon \vec{E} \right) = \rho \tag{10}$$

Charge continuity for a time-harmonic excitation can be expressed as (11).

$$\nabla \bullet \vec{J} = -j\omega\rho \tag{11}$$

Macroscopic Ohm's law can be expressed as (12).

$$\vec{J} = \sigma\vec{E} \tag{12}$$

Equation (13) is given by substituting (12) and (10) into (11).

$$\nabla \bullet \left(\sigma\vec{E}\right) + j\omega\left(\nabla \bullet \varepsilon\vec{E}\right) = 0 \tag{13}$$

The field can be expressed as the negative gradient of a scalar as in (14) since the curl of the electric field is zero according to (8).

$$\vec{E} = -\nabla\phi \tag{14}$$

Substituting (14) into (13) and collecting terms results in (15) which is the time-harmonic charge conservation equation and the governing differential equation for the frequency-dependent problem observed in this thesis.

$$-\nabla \bullet \left[\left(\sigma + j\omega\varepsilon\right)\nabla\phi\right] = 0 \tag{15}$$

C. Methods of Electrical Particle Force Calculations

Two methods for calculating particle electric force will be presented in this work. These are the Maxwell stress tensor integration and the effective dipole method. All finite element results are computed using the Maxwell stress tensor integration, while the effective dipole method will be used as a validation check for the finite element software package.

The effective dipole moment method of force calculation will first be presented. The effective dipole force is computed by substituting the polarization of the particle into the force expression for a dipole [11-12]. All spheres are approximated as cylinders since all particle force simulations in this work are two-dimensional. Therefore, it is necessary to understand the potential distribution for a cylindrical dielectric particle placed in a dielectric medium with an applied uniform electric field. Fig. 9 illustrates this scenario with a particle of radius R and dielectric constant of ε_2 in a medium with a dielectric constant of ε_1. A uniform electric field of strength E_0 is applied in the z-direction.
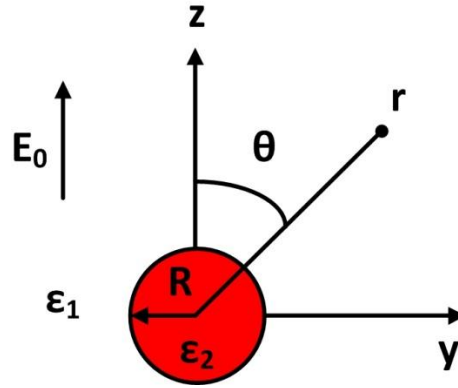
Fig. 9 Cylindrical particle in uniform electric field

The potential distribution for this problem is given in (16)-(19) where the subscript 1 indicates medium characteristics and the subscript 2 indicates particle characteristics [13].

$$\phi_1(r,\theta) = -E_0 r \cos(\theta) + A\frac{R}{r}\cos(\theta), \quad r>R \tag{16}$$

$$\phi_2(r,\theta) = B\frac{r}{R}\cos(\theta), \quad \text{r<R} \tag{17}$$

$$A = \frac{\varepsilon_2 - \varepsilon_1}{\varepsilon_2 + \varepsilon_1} RE_0 \tag{18}$$

$$B = \frac{-2\varepsilon_1}{\varepsilon_2 + \varepsilon_1} E_0 R \tag{19}$$

From (16-19), the interior field of the particle can be written in terms of the applied field as shown in (20).

$$\vec{E}_2 = \frac{2\varepsilon_1 \vec{E}_1}{(\varepsilon_1 + \varepsilon_2)} \tag{20}$$

The polarization of the particle can be defined as shown in (21).

$$\vec{P} = \varepsilon_0 (\vec{E}_2 - \vec{E}_1) V \tag{21}$$

Substituting (20) and the cylinder volume into (21) results in (22). This formula expresses the polarization of a dielectric cylinder in a uniform electric field.

$$\vec{P} = \varepsilon_0 \vec{E}_2 \left(\frac{\varepsilon_2 - \varepsilon_1}{\varepsilon_2 + \varepsilon_1} \right) (2\pi RL) \tag{22}$$

Fig. 10 displays a general dipole. The force on this dipole can be expressed as (23).
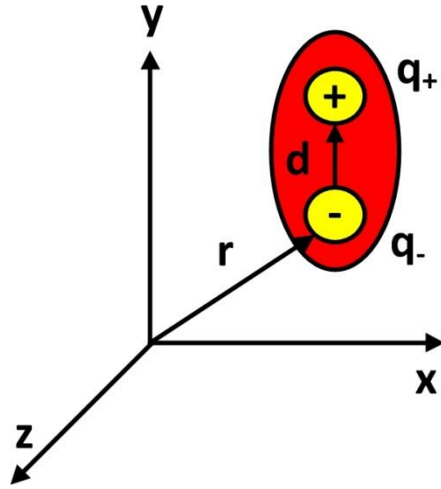
Fig. 10. General dipole illustration

$$\vec{F} = q\left[\vec{E}\left(\vec{r} + \vec{d}\right) - \vec{E}(\vec{r})\right] \tag{23}$$

The electric field can be expanded into a Taylor series about the negative charge point.

$$\vec{E}\left(\vec{r} + \vec{d}\right) = \vec{E}(\vec{r}) + \vec{d} \bullet \nabla \vec{E}(\vec{r}) + \dots \tag{24}$$

Substituting (24) into (23) results in (25). By defining the polarization as shown in (26), the force can be expressed as (27).

$$\vec{F} = q\vec{d} \bullet \nabla \vec{E} + \dots \tag{25}$$

$$\vec{P} = q\vec{d} \tag{26}$$

$$\vec{F} = \vec{P} \bullet \nabla \vec{E} + \dots \tag{27}$$

Substituting the polarization of the dielectric cylinder as shown in (22) results in (28).

$$\frac{\vec{F}}{L} = 2\pi R \varepsilon_1 \left(\frac{\varepsilon_2 - \varepsilon_1}{\varepsilon_2 + \varepsilon_1} \right) \vec{E}_2 \nabla \vec{E}_2 \tag{28}$$

By applying the vector identity (29), the dielectrophoretic force for a cylinder can be expressed as (30).

$$\vec{E}_2 \nabla \vec{E}_2 = \frac{1}{2} \nabla \left| \vec{E}_2 \right|^2 \tag{29}$$

$$\frac{\vec{F}}{L} = \pi R \varepsilon_1 \left(\frac{\varepsilon_2 - \varepsilon_1}{\varepsilon_2 + \varepsilon_1} \right) \nabla \left| \vec{E}_2 \right|^2 \tag{30}$$

The COMSOL program calculates force by the integration of the Maxwell stress tensor which is shown in (31). This stress tensor can be integrated along the particle boundary as in (32) to find the electric force on the particle.

$$T_{ij}^{\ E} = \varepsilon E_i E_j - \frac{\varepsilon}{2} \delta_{ij} E_k E_k \tag{31}$$

$$\vec{F} = \int_S \overline{\overline{T^E}} \bullet \hat{n} dA \tag{32}$$

D. COMSOL Electrical Force Computation Validation

It would be beneficial to validate the electrical results of COMSOL to establish the accuracy of the resulting solutions before proceeding on with this study. The force computation for the electric field will first be validated. Fig. 11 illustrates the validation problem. A potential drop of 1 V is applied across a torus with inner radius of 1m and outer radius of 5 m. A 0.2 m diameter particle with dielectric constant of 1000 was placed at the midpoint between the inner surface and the outer surface of the torus. The medium was assigned a dielectric constant of 2.1.
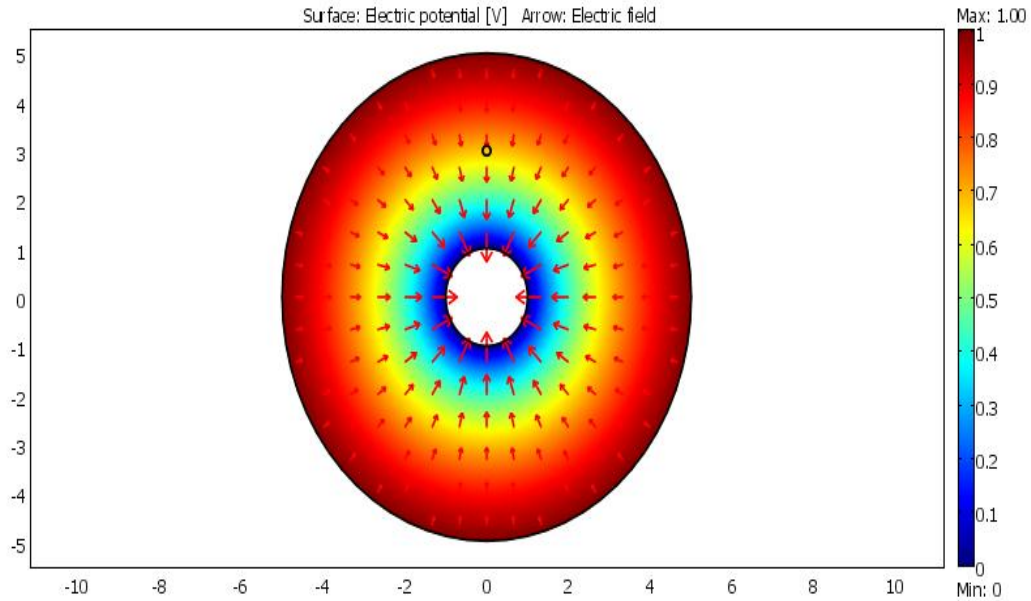
Fig. 11 Electrical force validation problem

The particle force was calculated according to (22) and compared with the finite element result which is shown in Table 1. There is good agreement between the two solution techniques.

Table 1: Finite element result vs. analytical effective dipole result

Analytical [N/m]	Finite Element [N/m]
-1.66e-14	-1.69e-14

E. COMSOL Fluidic Force Computation Validation

All fluidic flow was simulated under Stokes' flow conditions. The approximations for Stokes' flow are valid for low Reynold's number flows which are found in

microelectrode systems such as the ones modeled in this study [14]. The governing differential equation for Stokes' flow is given by (34).

$$0 = -\nabla P + \mu \nabla \bullet \nabla \vec{v} \tag{34}$$

The stress tensor for an incompressible, Newtonian fluid is given by (35).

$$T_{ij}^f = -P\delta_{ij} + \mu \left(\frac{\partial v_i}{\partial x_j} + \frac{\partial v_i}{\partial x_j} \right) \tag{35}$$

The fluidic force can be calculated by integrating this stress tensor as in (36).

$$\vec{F} = \int_S \overline{\overline{T^f}} \bullet \hat{n} dA \tag{36}$$

Fig. 12 illustrates the fluid force validation problem. A 0.125 m diameter spherical particle was placed in a fluidic flow of uniform velocity 1 m/s. The drag was computed according to (36).

Fig. 12. Fluid force validation problem

The finite element solution was compared with the Stokes' spherical drag solution with the results shown in Table 2. The two results agree quite well.

Table 2: Finite element result vs. spherical Stokes' flow analytical solution

Analytical [N/m]	Finite Element [N/m]
-1.88e-14	-1.88e-14

CHAPTER III

STUDY I: FORCE FREQUENCY DEPENDENCE

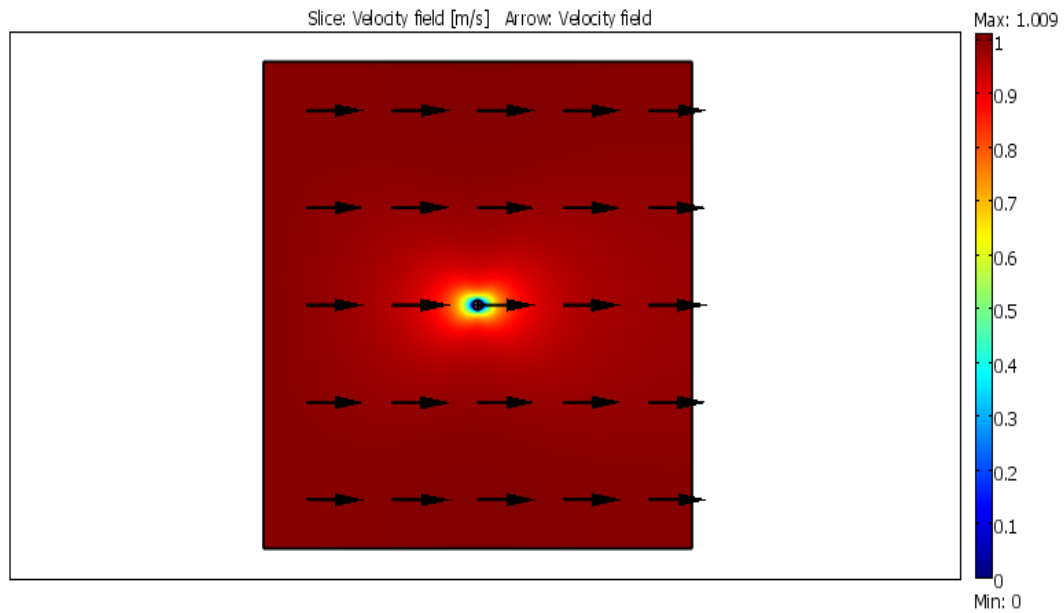***This chapter is dedicated to analyzing the electrokinetic behavior of a frequency-dependent experimental study involving coplanar parallel microelectrodes.*** This electrode geometry is used extensively and the analysis thereof will benefit colloidal assembly study on the whole. The understanding of particle force dependence on frequency provides insight into the resulting microstructure.

A. Introduction

Bahukudumbi *et al* [6] reported the results of their experiments with 800nm diameter gold colloids dispersed in aqueous 0.1 M NaHCO3 (conductivity of 9 μ S/cm). The experimental arrangement consisted of parallel 50 nm thick gold electrodes separated by 30 μ m on glass microscope slides. The gold colloids were confined within a thin, quasi-two-dimensional layer near the surface due to gravity and particle-surface electrostatic repulsion. The results were interpreted in terms of a competition between electrophoresis (EP), AC electro-osmosis (AC-EO), and dielectrophoresis (DP). Based on equations for the single-particle velocity as a function of frequency (ω) for each of those three phenomena, the authors postulated that EP dominates for $10^{-3} \leq \omega/\text{kHz} < 10^{0}$, AC-EO for $10^{-0} \leq \omega/\text{kHz} < 10^{1}$, and DP for $10^{-1} \leq \omega/\text{kHz} \leq 10^{4}$). The AC-EO domain widened with increasing magnitude of the electrode potential. The experimental colloidal configurations can be seen in Fig. 13. These results consist of a matrix filled with

elements of experimental results where higher elements indicate higher voltages and elements further to the right indicate higher frequencies. Note that the lower frequencies (10 Hz) show particles settling in the gap, middle frequencies (1 kHz) show particles being ejected from the gap, and the higher frequencies (above 100 kHz) show dielectrophoretic chaining.
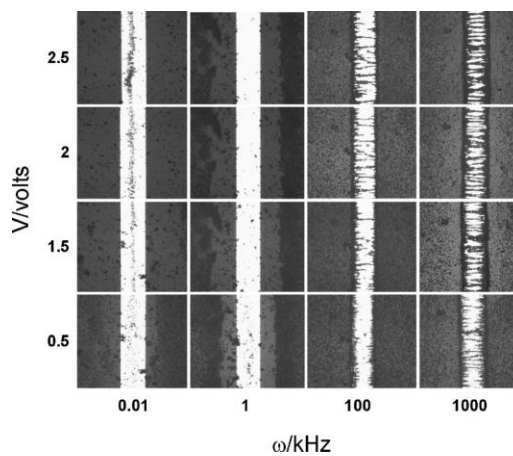
Fig. 13. Experimental colloidal microstructure [6]

The purpose of the research in this chapter is to further validate those conclusions by using the finite element method to model AC-EO and DP.

B. Problem Formulation

The problem domain, shown in Fig. 14, consists of an aqueous solution on two coplanar parallel electrodes. The solution is enclosed by glass except where the solution and electrodes form an interface. A two-dimensional problem was formulated by modeling the particles as cylinders infinitely extended in the direction normal to the figure.

Similarly, the electrodes were assumed to be infinitely extended in the direction normal to the figure. Note that Fig. 14 is an edge view of the domain, whereas Fig. 13 is a top view of the domain. The absolute value of the potential difference between the two electrodes was fixed at 2.5 V. The dielectric constants of the medium and particle were assigned values of 80 and 1 respectively. The conductivities of the medium and particle were 0.00573 S/m and $45.6*10^6$ S/m respectively.

Location	X (μm)	Y (μm)
1	1.2	3
2	40	3
3	90	3
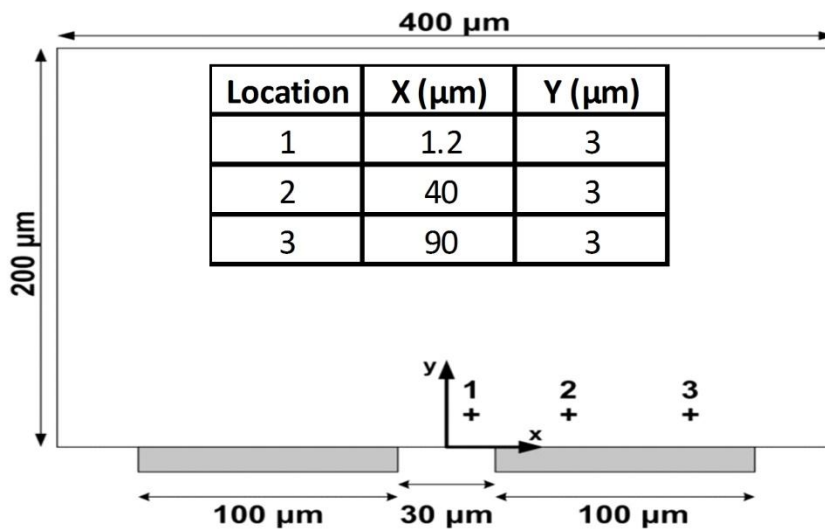
Fig. 14. 2D simulation domain where particles placed at positions 1,2, and 3
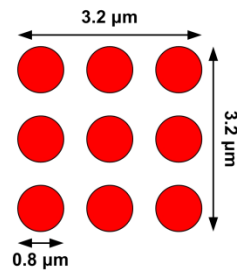
Fig. 15. 3x3 particle array

Two cases were modeled: single particles, and a 3x3 square array of particles (Fig. 15). The particle array is included to study the effects of multibody interactions. The distance between particle centers in the 3x3 array is 1.2 μ m in the x and y directions. The three locations in Fig. 14 correspond to the locations of single particles and the center particle of the 3x3 array. The three locations were studied sequentially rather than simultaneously, i.e., no particles were present at locations 2 and 3 when particles were at location 1, etc. The forces on the single particle or central particle, in the case of the array, were computed by integrating the Maxwell and Cauchy stress tensors on the particle surface. The mesh used to obtain the solution varied between 750,000 and 900,000 quadratic Lagrangian triangles.

The formulation of Green *et al.* for AC-EO was used for both the electrical and fluid problems [15]. In the bulk liquid the electric potential ϕ is governed by

$$\nabla \cdot ((\sigma + j\omega\varepsilon)\nabla\phi) = 0 \tag{37}$$

where $\sigma, \varepsilon,$ and ω are the conductivity, permittivity, and angular frequency. The following analysis assumes that electrolysis does not occur at the electrode surface, i.e., the electrodes are considered to be perfectly polarizable, and the double layer behaves in a linear manner. The boundary condition just outside the double layer on the electrode surface is given by

$$\sigma \frac{\partial \phi}{\partial n} = \frac{\partial q_{DL}}{\partial t} \tag{38}$$

where n denotes the unit normal vector and q_{DL} is the charge per unit area in the double

layer. In this equation it is assumed that tangential currents along the double layer are

negligible. If the voltage drop across the diffuse double layer is sufficiently small, there

is a linear relationship between the charge and the voltage, i.e., $q_{DL} = C_{DL}\Delta\phi_{DL}$, where

$\Delta\phi_{DL} = \phi - V$, and the equation can be written with complex amplitudes as (39).

$$\sigma\frac{\partial\phi}{\partial n} = i\omega q_{DL} = i\omega C_{DL}\Delta\phi_{DL} \tag{39}$$

where C_{DL} is the capacitance per unit of area of the total double layer, and V is the

potential applied to an electrode, and ϕ is the potential on the outer side of the diffuse

layer. The capacitance per unit area can be estimated from the Debye-Huckel theory as

$$C_{DL} = \frac{\varepsilon}{\lambda_D} \tag{40}$$

where λ_D is the Debye length which is widely used to estimate the double layer

thickness given by (41).

$$\lambda_D = \sqrt{\frac{\varepsilon kT}{2z^2e^2c_b}} \tag{41}$$

where k, T, z, e and c_b are Boltzmann constant, absolute temperature, valence of ion,

electron charge and concentration of ions, respectively. At the interface between the

electrolyte and the glass, the total normal electric displacement must be continuous.

$$(i\omega\varepsilon + \sigma)\frac{\partial\phi}{\partial n} = (i\omega\varepsilon_G + \sigma_G)\frac{\partial\phi_G}{\partial n} \tag{42}$$

where ε_G, σ_G and ϕ_G are the electrical permittivity, conductivity and potential in the glass. Since $\omega \ll \sigma/\varepsilon < \sigma/\varepsilon_G$ and the conductivity of the glass is negligible, the boundary condition at the glass interface in the fluid simplifies to

$$\frac{\partial \phi}{\partial n} = 0 \tag{43}$$

The time averaged Maxwell stress tensor is given by (44).

$$\left\langle \overline{\overline{T^E}} \right\rangle = \frac{1}{2} \operatorname{Re}\left[\varepsilon \vec{E} \vec{E}^{*\mathbf{T}} - \frac{1}{2}\left(\varepsilon \vec{E} \cdot \vec{E}^* \right)\overline{\overline{I}} \right] \tag{44}$$

The fluid motion is caused by electrical body forces that are nonzero only in the diffuse double layer since the charge density in the bulk is zero. These forces result in a rapidly varying velocity profile in the diffuse double layer, changing from zero at the wall to a finite value just outside the double layer. This velocity value can be used as a boundary condition at the electrode surface to calculate the bulk motion. In the thin double layer approximation, for diffuse layers in quasiequilibrium and on a perfectly polarizable metal surface, the slip electro-osmotic velocity is given by the Helmholtz-Smoluchowski formula

$$u_t = -\frac{\varepsilon}{\eta} \Delta\phi_{DL} \frac{\partial \phi}{\partial x} \tag{45}$$

where η is the fluid viscosity. The Helmholtz-Smoluchoswki time averaged AC electroosmosis fluid velocity is given by

$$u_{t,ACE} = \langle \vec{u} \rangle = -\frac{\varepsilon}{2\eta} \operatorname{Re}\left[\Delta\phi_{DL} \frac{\partial\phi^*}{\partial x} \right] \tag{46}$$

where ϕ^* is the complex conjugate of ϕ. The bulk fluid is governed by Stokes flow of which the governing equations are given by (47) and (48).

$$\eta\nabla^2 \langle \vec{u} \rangle - \nabla p = 0 \tag{47}$$

$$\nabla \cdot \langle \vec{u} \rangle = 0 \tag{48}$$

where p is the pressure. The mechanical stress tensor is given by

$$\left\langle \overline{\overline{T^f}} \right\rangle = -\langle p \rangle \overline{\overline{I}} + \eta\left(\nabla\langle \vec{u} \rangle + (\nabla\langle \vec{u} \rangle)^{\mathbf{T}} \right) \tag{49}$$

and the traction vector is given by (50).

$$\langle \vec{t} \rangle = \left(\left\langle \overline{\overline{T^f}} \right\rangle + \left\langle \overline{\overline{T^E}} \right\rangle \right)\hat{n} \tag{50}$$

The boundary conditions are (i) the tangential AC electro-osmotic velocity on the electrodes, equation (10); (ii) zero tangential velocity on the glass; (iii) zero normal velocity on every boundary; and (iv) continuous traction vector on all interfaces

$$\left| \langle \vec{t} \rangle \right| = 0 \tag{51}$$

where $\left| \langle \vec{t} \rangle \right|$ is the jump in the time averaged traction vector at any interface.

C. Results and Discussion

The present problem was solved, with the numerical results given in Tables 3 and 4, which contain the x and y components of the electrical force, F_{ex} and F_{ey}, the fluid force, F_{fx} and F_{fy}, and the x and y components of the total force obtained by summing the electrical and fluid forces. Fig. 16 displays the typical streamline and potential distribution for the simulations where red indicates high potential and blue indicates low potential. Fig. 17 displays the force vectors for the single particle case on a logarithmic scale.
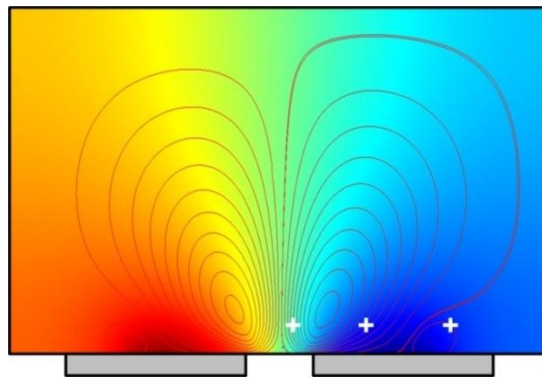
Fig. 16. Typical streamlines and potential distribution

Table 3. Single particle forces in microelectrode domain

Location	Freq (Hz)	Fex (N/m)	Fey (N/m)	Ffx (N/m)	Ffy (N/m)	Ftotalx (N/m)	Ftotaly (N/m)
1	10	6.35E-15	-1.21E-14	4.11E-12	-8.44E-12	4.12E-12	-8.45E-12
	1.00E+03	2.48E-11	-4.95E-11	1.15E-08	-2.36E-08	1.15E-08	-2.36E-08
	1.00E+05	1.76E-10	-4.22E-10	1.80E-09	-3.82E-09	1.98E-09	-4.24E-09
2	10	-5.03E-13	-6.52E-13	2.87E-09	3.98E-10	2.87E-09	3.97E-10
	1.00E+03	-2.30E-09	-2.53E-09	6.97E-06	1.19E-06	6.97E-06	1.19E-06
	1.00E+05	-4.79E-09	-8.52E-10	5.62E-08	1.22E-08	5.14E-08	1.13E-08
3	10	-5.06E-15	-5.67E-13	2.84E-10	1.73E-10	2.84E-10	1.72E-10
	1.00E+03	3.18E-12	-1.26E-09	3.78E-07	3.80E-07	3.78E-07	3.79E-07
	1.00E+05	1.28E-10	-2.23E-10	-1.52E-09	1.17E-09	-1.39E-09	9.47E-10

Fig. 17. Normalized single particle force vectors as a function of frequency

Table 4. Particle array forces in microelectrode domain

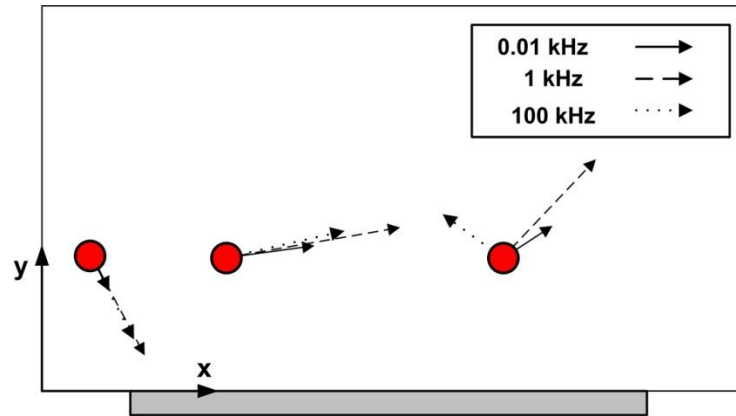| Location	Freq (Hz)	Fex (N/m)	Fey (N/m)	Ffx (N/m)	Ffy (N/m)	Ftotalx (N/m)	Ftotaly (N/m)
	10	2.04E-13	2.25E-13	1.34E-11	-3.18E-11	1.36E-11	-3.16E-11
1	1.00E+03	8.18E-10	6.73E-10	3.77E-08	-8.92E-08	3.85E-08	-8.85E-08
	1.00E+05	5.99E-09	4.79E-11	6.65E-09	-1.46E-08	1.26E-08	-1.46E-08
	10	-4.67E-13	-3.04E-13	3.94E-10	7.51E-11	3.94E-10	7.48E-11
2	1.00E+03	-1.77E-09	-1.48E-09	9.58E-07	2.21E-07	9.56E-07	2.20E-07
	1.00E+05	-2.76E-09	-4.19E-09	6.30E-09	-2.54E-09	3.54E-09	-6.73E-09
	10	2.96E-15	-3.06E-13	3.58E-11	2.88E-11	3.58E-11	2.85E-11
3	1.00E+03	1.10E-11	-5.87E-10	4.51E-08	5.81E-08	4.51E-08	5.75E-08
	1.00E+05	6.11E-11	-1.15E-09	-1.94E-10	-1.19E-09	-1.33E-10	-2.34E-09

The results in Tables 3 and 4 are supported by the experimental observations of Fig. 13. The fluid forces are largest for the intermediate frequency (1kHz) and smaller for the low (10Hz) and high (100kHz) frequencies.

The fluid force reaches its highest value at the 1 kHz frequency for all particle locations. The electric force is the highest at the 100 kHz frequency for all particle locations. However, the fluid force is greater than the electric force at all frequencies.

For particle locations 1 and 2, the force F_{totalx} is weakest, strongest, and intermediate for 10 Hz, 1kHz, and 100 kHz, respectively. For particle location 3, the force increases from 10Hz to 1kHz and then reverses direction for 100kHz. At 1kHz, the particles are forced to the right at all frequencies, in agreement with Fig. 13 that shows the particles accumulating on the right half of the electrode.

Fig. 13 demonstrates that at 10Hz the particles accumulate near x=0. Thus, F_{totalx} at location 1 should be to the left. In contrast, the current simulation predicts that F_{totalx} at location 1 is to the right, but the force is very small, indicating stagnation and particle accumulation. At 100kHz, at particle location 2, F_{totalx} is to the right, whereas F_{totalx} is to the left at location 3. This is supported by the accumulation of particles at the innermost electrode edge in Fig. 13.

The force on the center particle of the array is reversed, in some cases, with respect to the force on a single particle. For example, at location 1 at 1kHz and 100kHz, F_{ey} is upward for the center particle and downward for the single particle. However F_{fy}, which is the dominate term, is downward at location 1 in all cases. A more significant difference between the center particle and the single particle results occurs at locations 2 and 3 for the case of 100kHz, in which F_{fy}, a significant force, is downward for the center particle and upward for the single particle.

Finally, it is noted that the sedimentation force F_{sed} , which is in the y direction, is equal to:

$$F_{sed} = -(\rho_{gold} - \rho_{solute})g\frac{4}{3}\pi R^3 = -4.81\text{x}10^{-14} N/m \tag{52}$$

which is negligible compared to F_{totaly} for all cases considered.

The electric and fluid forces calculated by integrating the Maxwell and Cauchy tensors on the surface of a particle provide insight into the equilibrium configuration of the particles. The results support the conclusions of Bahukudumbi *et al* [6] concerning their experiments with 800nm diameter gold colloids dispersed in aqueous 0.1mM NaHCO3: for 2.5V magnitude, AC-EO dominates for intermediate frequencies and DP for higher frequencies. The fluid forces calculated from FEA are largest for the intermediate frequency (1kHz) and smaller for the low (10Hz) and high (100kHz) frequencies. The electric forces are largest for the high (100 kHz) frequency. Also, the sedimentation force is much smaller than the electric and fluid forces.

D. Key Insights and Contributions

The simulation results show good agreement with the experimental results. The particles experience larger forces pointing away from the gap at the intermediate frequency (1 kHz) indicating larger AC electroosmotic force at this frequency. The particles start to experience smaller forces pointing away from the gap and even some forces pointing toward the gap indicating a weakening in the AC electroosmotic force at the high (100

kHz) frequency. The electric force also reaches its largest value at the high frequency indicating a transfer from AC electroosmosis dominance to dielectrophoresis dominance. The frequency regimes dominated by AC electroosmosis will form colloidal systems with particles ejected from the gap, while those dominated by dielectrophoresis will form particle chains between the electrodes. ***This study has demonstrated the simulation method's ability for capturing colloidal microstructure behavior in AC fields.***

CHAPTER IV

STUDY II: FORCE PARTICLE SHAPE DEPENDENCE

This chapter builds on the confidence that finite element simulations can be used to predict the electrokinetic behavior and uses this to analyze the shape-effects of aspect ratio on interparticle forces between colloidal particles. Insight into the conditions necessary for higher aspect ratio particle attraction can be obtained from this force analysis. Radial force analysis between two particles can indicate regions of attraction, while the overall force magnitude indicates the degree of attraction.

A. Introduction

Dielectric particles will repel one another when they are orthogonally oriented to the applied as shown in Fig. 18. The particles will attract one another when they are oriented along the field direction as shown in Fig. 19. There is an angle of transition between the parallel and perpendicular orientations in which the two particles will switch from attracting to repelling one another as shown in Fig. 20. This angle will hereafter be referred to as θ_{cr}.
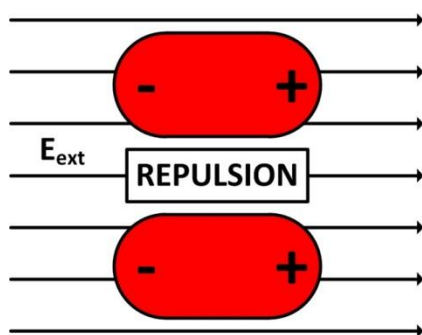
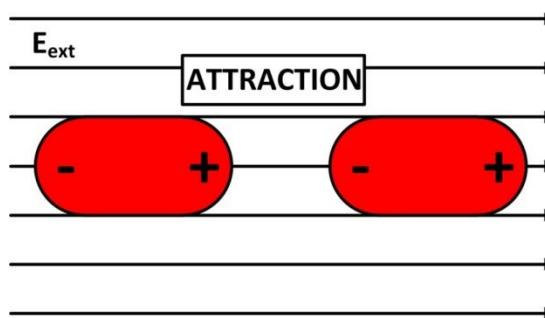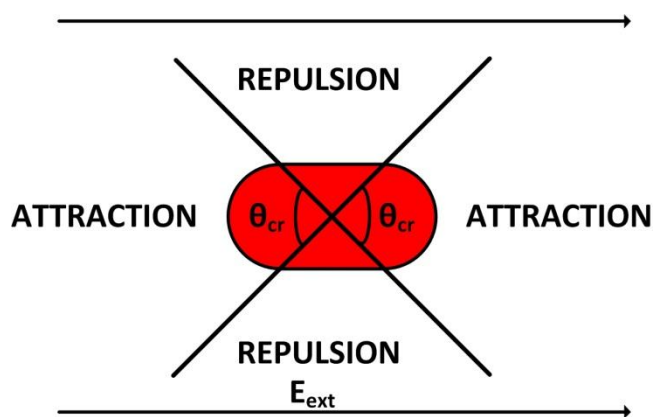Fig. 18. Particle repulsion in perpendicular orientation

Fig. 19. Particle attraction in parallel orientation

Fig. 20. Regions of attraction and repulsion defined by θ_{cr}

The analytical dipole approximation for the interparticle force between two spherical dielectric particles in a uniform electric field can be found in Parthasarthy *et al.* [16].

$$F_{ij} = \frac{3}{16}\pi\varepsilon_1\beta^2 E_0^2 \left(\frac{R}{D_{ij}}\right)^4 \left[(3\cos^2\theta_{ij}-1)\hat{e}_r + (\sin 2\theta_{ij})\hat{e}_\theta\right] \qquad (53)$$

$$\beta = \frac{\varepsilon_2 - \varepsilon_1}{\varepsilon_2 + 2\varepsilon_1} \qquad (54)$$

where ε_2, ε_1, E_0, R, D_{ij}, and θ_{ij} are particle permittivity, medium permittivity, applied field magnitude, particle radius, separation distance, and angle of separation vector with respect to electric field direction, respectively, as shown in Fig. 21 where the field is applied in the z-direction.
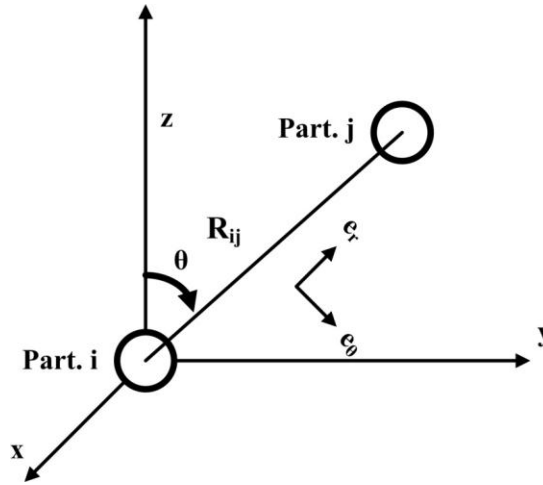

Fig. 21. Interparticle force expression geometry [16]

The θ_{cr} value for spherical particles can be found by calculating the root of the radial component in (57). The result of this analysis produces a θ_{cr} value of 54.8° for spherical dielectric particles. The goal of this study is to find these θ_{cr} values for higher aspect

ratio particles and to examine the angular dependency of interparticle force at large aspect ratios.

B. Problem Formulation

The problem domain consists of TiO_2 particles embedded in silicone oil with an applied uniform, unidirectional field of strength 10^6 V/m. These particles were modeled as 2d cylinders to limit computational complexity. The particles and silicone oil were assigned dielectric constants of 130 and 2.1, respectively.

The edge separation distance is defined in Fig. 22. Aspect ratio change is performed by stretching the particle with fixed height and semicircular arcs on each end until the desired aspect ratio is reached. Simulations were performed for aspect ratios of 1, 5, and 12.92 as well as edge separation distances of 0.25 µm, 0.50 µm, and 2.0 µm and angles of 0º - 90º in 22.5º increments. The 12.92 aspect ratio and 2.0 µm edge separation distance were chosen to match an ongoing colleague's experiment which is unpublished.
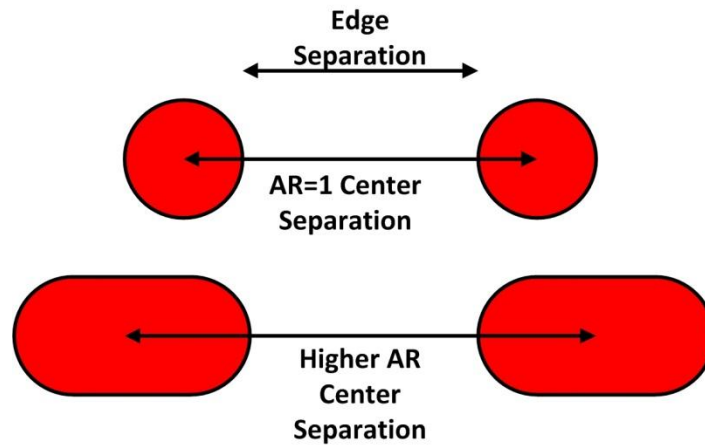
Fig. 22. Edge separation definition

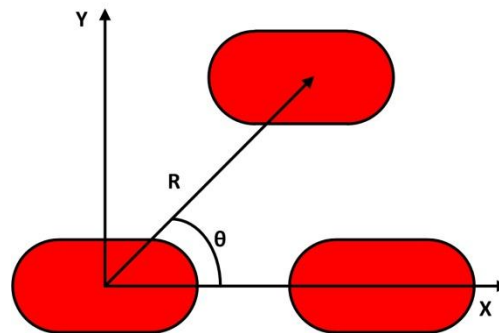The simulations were performed using the following procedure (see Fig. 23):

Fig. 23. Shape effects simulation procedure illustration

(1) The finite element program calculates interparticle force for two TiO_2 particles with the same given aspect ratio and given edge separation distance in a uniform electric field of strength 10^6 V/m.

(2) Outer particle rotates to a new θ position as shown in Fig. 23. Interparticle force is recalculated. This is repeated for all angular positions.

(3) Edge separation distance is changed and Step (2) is performed for the new separation distance. This is repeated for all edge separation distances. Step (4) is then executed.

(4) Aspect ratio is changed and Steps (1)-(3) are repeated for each aspect ratio.

C. Results and Discussion

The forces calculated in this analysis were highly mesh dependent. Simple mesh refinement in terms of total number of elements would not produce converged results. An extensive convergence study was performed. It was determined that a symmetric, high-density mesh around the boundary of the particle was required to obtain good convergence. Converged results were obtained using these symmetric meshes.

Fig. 24 shows the radial force component as a function of aspect ratio and edge separation. The force components are defined in such a way that a negative radial component indicates particle attraction and a positive radial component indicates particle repulsion. The maximum attractive force is greater than the maximum repulsion force for all cases. Circular particles yield similar values for θ_{cr} at all separation distances.

Separation distance has a greater effect on θ_{cr} as the aspect ratio increases. Note that higher aspect ratio particles produce larger interparticle attractive forces.

Table 5 displays the θ_{cr} values in tabular form for each aspect ratio and separation distance. Lower aspect ratio particles produce larger critical angle values for a given separation distance. The difference between θ_{cr} values at various edge separation distances is smaller for lower aspect ratio particles.

Table 5. θ_{cr} vs. aspect ratio at various edge separations

	Edge Separation	θ_{cr}
	0.25 μm	46.8°
AR = 1	0.50 μm	45.5°
	2.00 μm	45.0°
	0.25 μm	36.7°
AR = 5	0.50 μm	39.5°
	2.00 μm	43.9°
	0.25 μm	27.4°
AR = 12.92	0.50 μm	32.9°
	2.00 μm	40.5°

Figs. 25 and 26 present the tangential force component and total force magnitude as functions of aspect ratio and edge separation distance. Circular particles produce symmetric tangential force curves around 45° similar to the tangential force component of (57). Larger aspect ratio particles produce tangential force curves that are skewed to the left (i.e. larger tangential forces for angles less than 45°). Larger aspect ratio particles also produce larger force magnitudes between the particles.
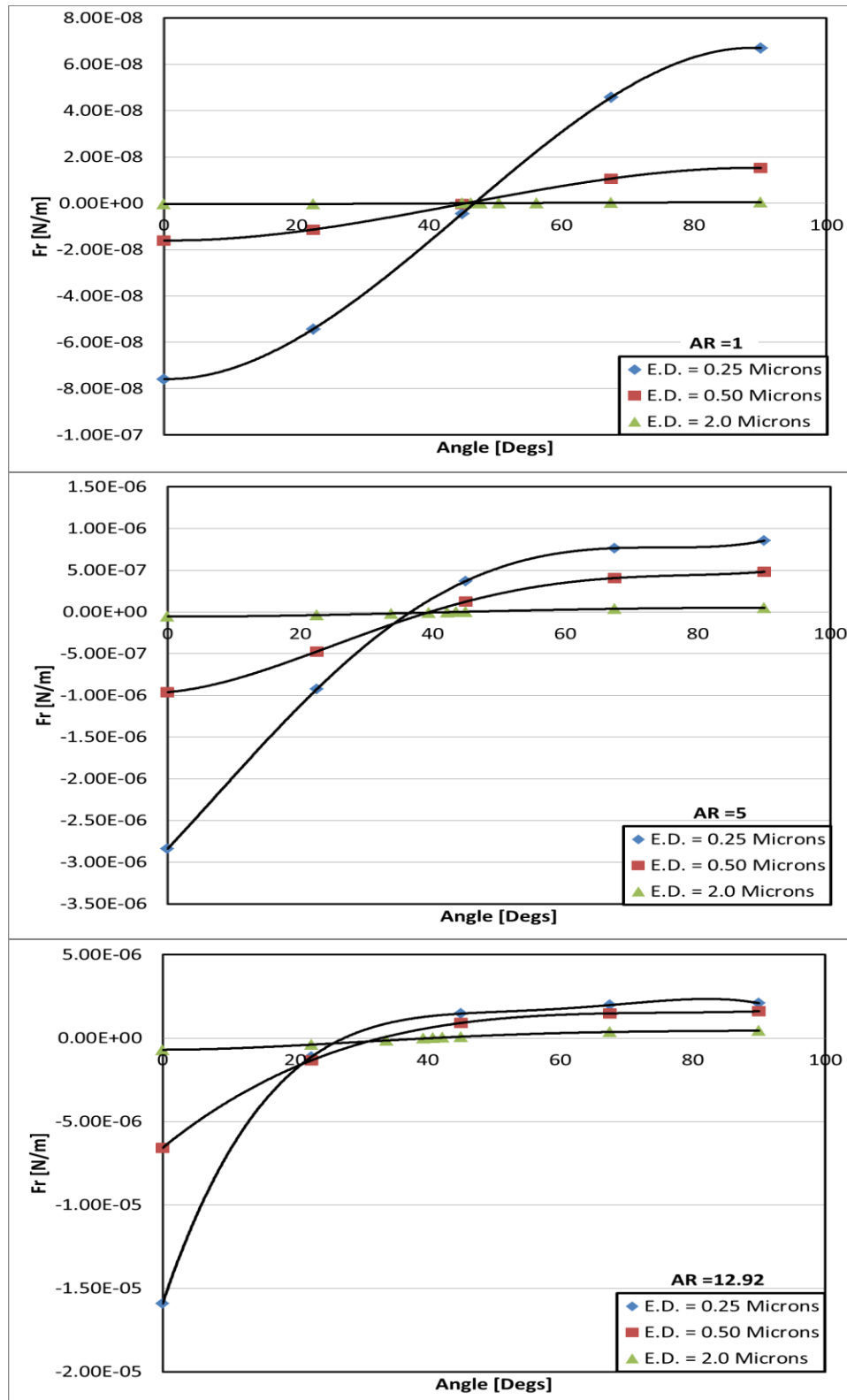
Fig. 24. Radial force vs. aspect ratio and edge separation distance
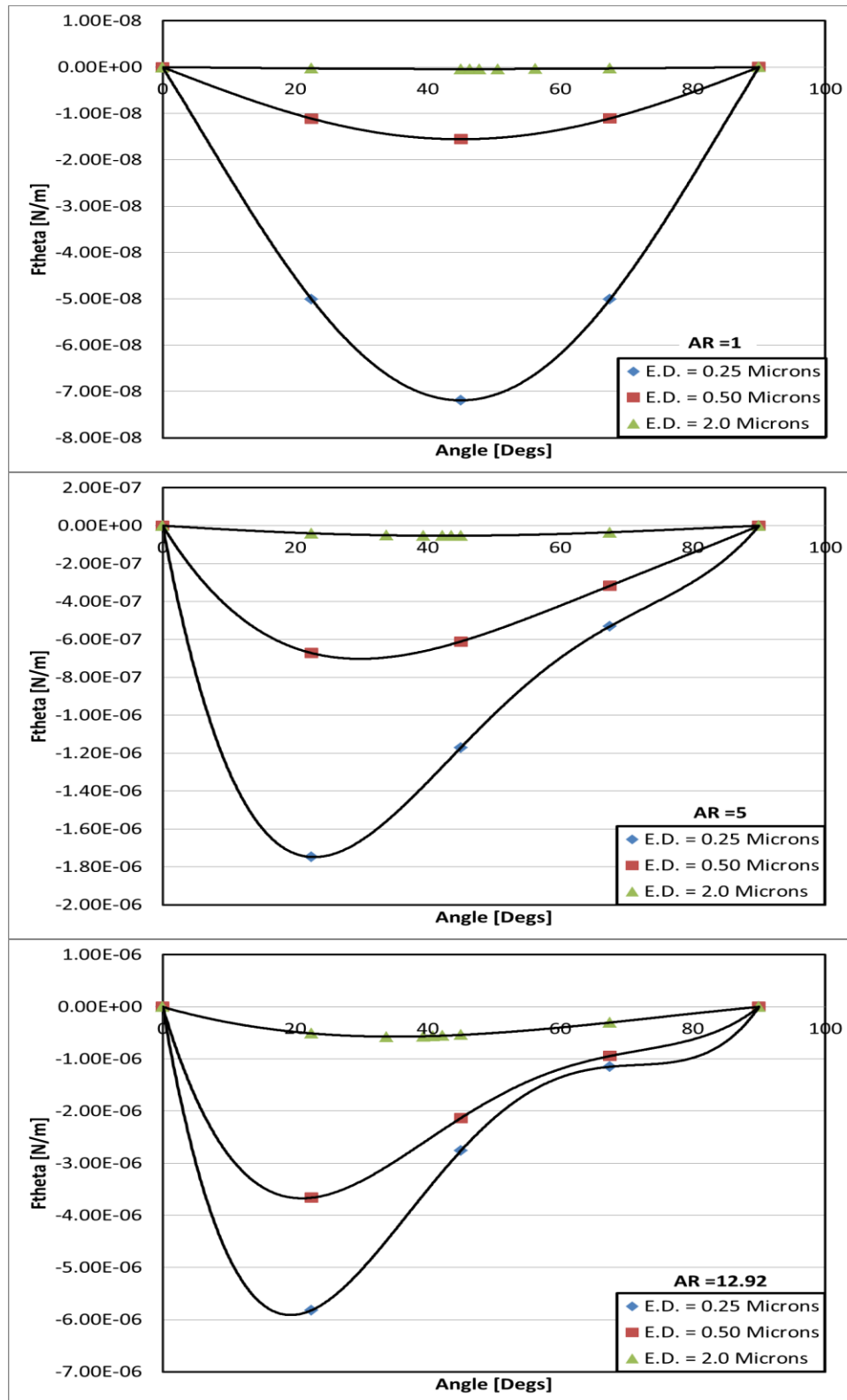
Fig. 25. Tangential force vs. aspect ratio and edge separation distance
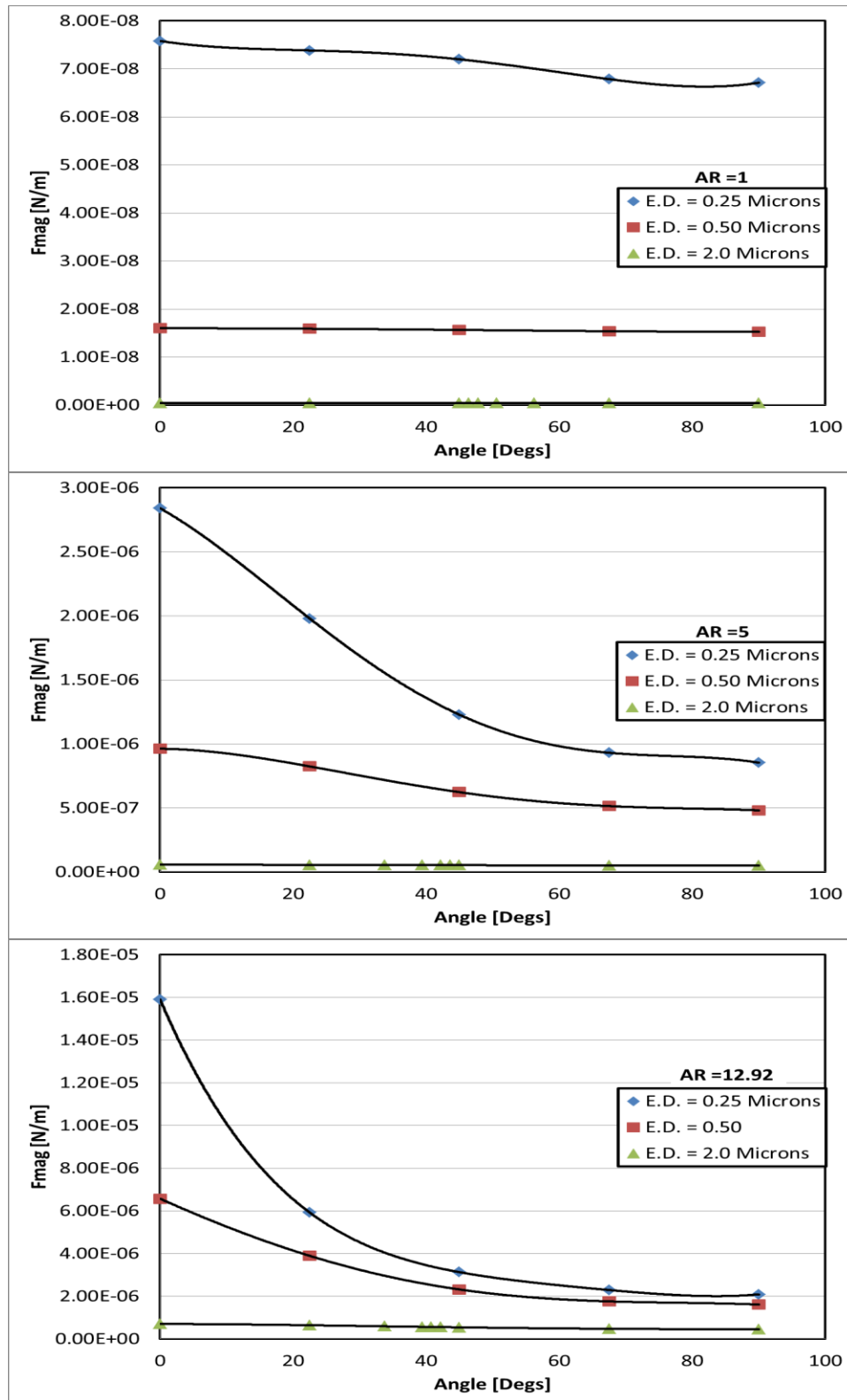
Fig. 26. Force magnitude vs. aspect ratio and edge separation distance

D. Key Insights and Contributions

The simulations in this chapter have shown that larger aspect ratio particles produce higher attractive forces but smaller θ_{cr} values. Particles attract one another when the angle formed by the line between their centers and the field direction is less than θ_{cr}. Therefore, larger aspect ratio particles will have smaller regions of attraction than lower aspect ratio particles. This provides insight into chaining because particles that are in the attractive regions of one another will form chains, while those in the repulsion regions will be pushed to the attraction region of another particle. ***In a broader context, this chapter has provided one of the first studies on the impact of particle morphology and used this to develop numerical methods which can be applied to characterize the fundamental electrokinetic behavior of these particles.***

CHAPTER V

STUDY III: EFFECTIVE PROPERTIES SIMULATIONS

This chapter also investigates the properties of microstructured nanoparticles but is dedicated to the effective medium analysis of colloidal dispersions using periodic lattices. The simulation method will be compared to a classical mixing rule for simple geometries. The simulation method will then be used to analyze a more complex geometry with no analytical, closed-form solution.

A. Introduction

An effective dielectric constant finite element analysis of BSTO particles in silicone oil was performed for various particle configurations and volume fractions. These configurations consist of simple-cubic and face-centered cubic (FCC) lattices. The effective properties were calculated using techniques illustrated in Lee *et al.* [8]. These resultant effective properties were then compared with the Maxwell Garnett mixing rule, a well-known and established formula for computing effective properties. This mixing rule does not take into account field perturbations due to multibody interactions. It will become inaccurate at higher volume fractions. Less canonical structures of cubic particle lattices were analyzed after comparison of simpler geometries to the Maxwell Garnett mixing rule.

B. Problem Formulation

The problem domain consists of 100 nm diameter BSTO particles embedded in a silicone oil liquid medium. The particles and oil were assigned dielectric constant values of 1000 and 2.1, respectively. It was assumed that both constituents are linearly polarizable. The basic constitutive relation for a linearly polarizable material is:

$$\vec{D} = \varepsilon\vec{E} \tag{55}$$

Expanding Eqn. (55) into matrix notation for Cartesian coordinate system gives (56).

$$\begin{bmatrix} Dx \\ Dy \\ Dz \end{bmatrix} = \begin{bmatrix} \varepsilon_{xx} & \varepsilon_{xy} & \varepsilon_{xz} \\ \varepsilon_{yx} & \varepsilon_{yy} & \varepsilon_{yz} \\ \varepsilon_{zx} & \varepsilon_{zy} & \varepsilon_{zz} \end{bmatrix} \begin{bmatrix} Ex \\ Ey \\ Ez \end{bmatrix} \tag{56}$$

The method used in Lee *et al.* [8] for calculating effective properties involves taking a representative volume element from the overall domain, applying a field in each coordinate direction singularly, and then computing the volume-averaged electric displacement. It is possible to solve the matrix equation shown in (56) for the material property tensor from the calculated electric displacement. Equation (56) reduces to (57) by applying an x-directed field and computing the electric displacement volume average as shown in (58):

$$\begin{bmatrix} \langle Dx \rangle \\ \langle Dy \rangle \\ \langle Dz \rangle \end{bmatrix} = \begin{bmatrix} \varepsilon_{xx} \\ \varepsilon_{yx} \\ \varepsilon_{zx} \end{bmatrix} \begin{bmatrix} Ex \end{bmatrix} \tag{57}$$

where

$$\langle D\alpha \rangle = \frac{1}{V} \int D\alpha dV \qquad \alpha = x, y, z \tag{58}$$

Equation (57) shows that ε_{xx}, ε_{xy}, and ε_{xz} can be calculated when the average electric displacement components are known. The other components of the tensor can be found similarly by applying fields in the other two coordinate directions. This procedure was implemented to calculate the effective permittivity tensor for various volume fractions for both simple cubic and face centered cubic particle configurations. The volume fraction was varied by keeping the particle radius constant and changing the representative volume element dimensions.

The Maxwell Garnett mixing rule for calculating the effective medium permittivity is shown in (59).

$$\varepsilon_{eff} = \varepsilon_1 + 3f\varepsilon_1 \frac{\varepsilon_2 - \varepsilon_1}{\varepsilon_2 + 2\varepsilon_1 - f(\varepsilon_2 - \varepsilon_1)} \tag{59}$$

where ε_1, ε_2, ε_{eff}, and f represent the medium permittivity, inclusion permittivity, effective permittivity, and volume fraction, respectively.

C. Results and Discussion

Figs. 27 and 28 show the results for simple cubic and FCC crystal structures with spherical particles. Good agreement exists between the Maxwell Garnett rule and the finite element results for both lattice structures below 30% volume fractions (less than 2% error) The FCC results agree with the Maxwell Garnett mixing rule better than the simple cubic results at volume fractions over 30%. The FCC results and Maxwell Garnett results show less than 9% difference at these higher volume fractions (up to 60%). FCC lattices have larger particle separation distances than simple cubic lattices for a given volume fraction. Therefore, the FCC results should agree more closely with the Maxwell Garnett mixing rule because there is less multibody field interaction in the FCC structure.

f	COMSOL	MG	% Error
0.10	2.79	2.80	0.18
0.20	3.67	3.66	0.20
0.30	4.87	4.78	1.97
0.40	6.79	6.26	8.53
0.45	8.47	7.20	17.70
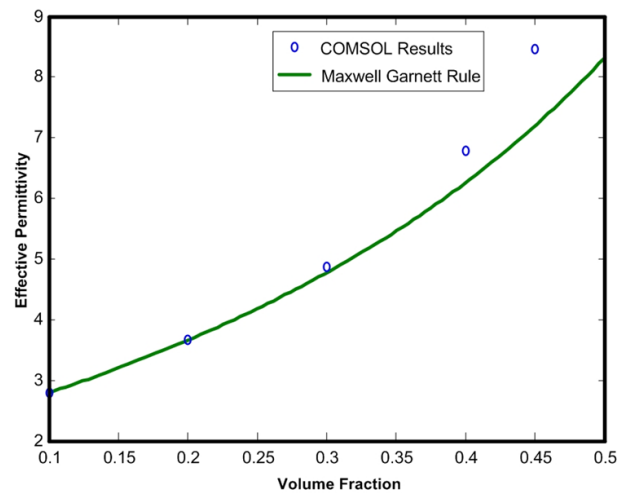
Fig. 27. Simple cubic effective property modeling results

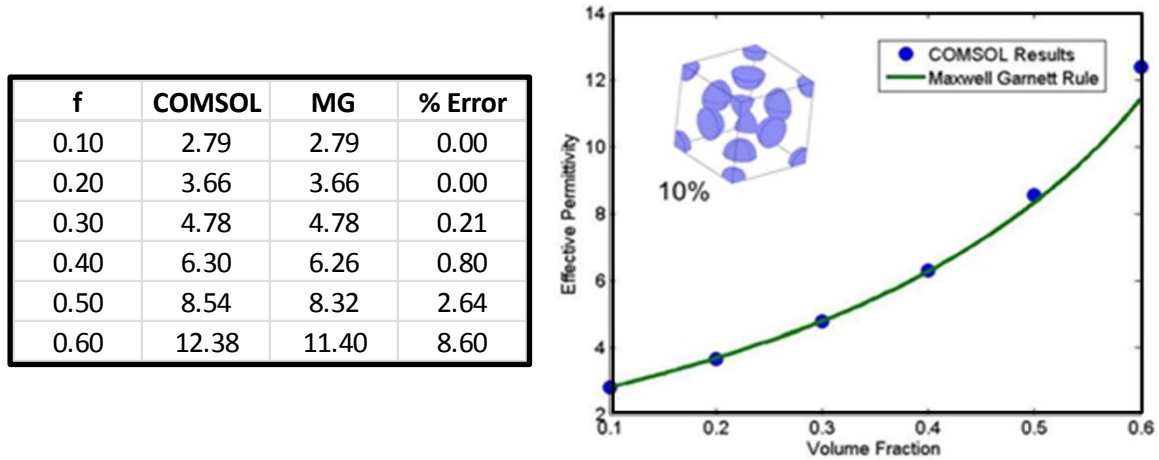| f	COMSOL	MG	% Error
0.10	2.79	2.79	0.00
0.20	3.66	3.66	0.00
0.30	4.78	4.78	0.21
0.40	6.30	6.26	0.80
0.50	8.54	8.32	2.64
0.60	12.38	11.40	8.60

Fig. 28. FCC effective property modeling results

An accurate effective property modeling technique should agree with the Maxwell Garnett mixing rule at lower volume fractions and start to deviate at higher volume fractions. The technique shown here meets this condition. A more exotic cubic particle geometry was analyzed after gaining confidence from the relatively simple spherical particle geometries. There is no closed-form analytical mixing rule for these cubic particles. This is the area in which this simulation method can prove its utility. Simulations were performed with the simple cubic lattice structure with cubic particles of side length 100 nm. Fig. 29 shows the comparison of the cubic and spherical particles arranged in a simple cubic lattice. The cubic particles produced higher dielectric constants for given volume fractions up to around 40%. The spherical particles started to produce higher dielectric constants past this point.

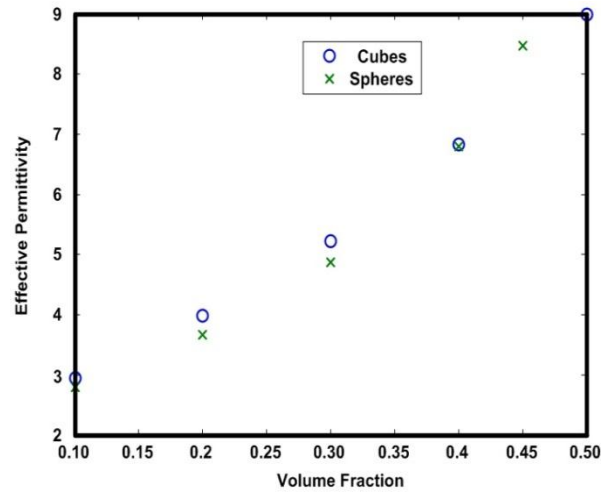| f	Spherical	Cubic
0.10	2.79	2.95
0.20	3.67	3.98
0.30	4.87	5.23
0.40	6.79	6.83
0.45	8.47	8.32
0.50	Convergence Issues	9.00

Fig. 29. Comparison of spherical and cubic particle effective properties

D. Key Insights and Contributions

The finite element simulation method showed good agreement with the Maxwell Garnett mixing rule for both the simple cubic and FCC lattice structures. The FCC lattice structure results show better agreement with the Maxwell Garnett mixing rule than the simple cubic lattice primarily due to the increased spacing of the FCC structure. The simulation method presented in this chapter agrees well with the Maxwell Garnett mixing rule at low volume fractions and starts to deviate slightly at higher volume fractions. These are two indicators of an accurate effective medium simulation method. ***The true utility of a method such as this lies in complex geometries with no mixing rule such as the cubic particles studied here.***

CHAPTER VI

ONGOING AND FUTURE WORK

The ongoing and future work will be primarily composed of two areas. The first will be performing finite element effective property simulations using lattices with random periodic particle distributions. The code for generating the random periodic crystal lattice has already been developed and some preliminary results have been found but more iterations need to be performed for averaging.

The second area involves dynamic particle simulations using the finite element method [17]. The forces computed on the particles in this study will be output into an ordinary differential equation of motion to be solved numerically. The particle will move to a new location based on this motion equation so the mesh will be updated to reflect the new geometry. The new force for the new location will then be calculated using the same methods in this thesis. This process will be repeated so that the particle trajectories can be computed.

CHAPTER VII

CONCLUSION

This work has examined frequency and particle shape effects on interparticle forces, as well as effective medium properties of colloidal systems. Each study provides insight into the behavior of colloidal particles under the influence of electric fields. Study I examined the frequency-dependent behavior of gold colloidal nanoparticles influenced by electric fields. The study validates the conclusions drawn by Bahukudumbi *et al*; namely, the frequency spectrums at which electroosmotic and dielectrophoretic forces dominate. The identification of which phenomena dominates yields knowledge of the resulting colloidal microstructure. Study II examines the aspect ratio dependence of interparticle force. Higher aspect ratio particles had both higher force magnitudes and smaller attractive regions than lower aspect ratio particles. This provides insight into the how the conditions of particle attraction vary based on aspect ratio. Study III examines an effective method for computing the average homogenized properties of colloidal systems. The results showed good agreement with the Maxwell Garnett mixing rule. This gives confidence in the method to simulate exotic structures with no closed-form mixing rules such as the cubic particle system analyzed.

REFERENCES

1. T. C. Halsey, "Electrorheological Fluids," *Science,* vol. 258, pp. 761-766, 1992.

2. S. A. Goldberger, "A study of microfluidic reconfiguration mechanisms enabled by functionalized dispersions of colloidal material for radio frequency applications," Master of Science, Electrical Engineering, Texas A&M University, College Station, Texas, 2010.

3. J. Nikitczuk, B. Weinberg, and C. Mavroidis, "Rehabilitative knee orthosis driven by electro-rheological fluid based actuators," *Proceedings of the 2005 IEEE International Conference on Robotics and Automation*, 2005, pp. 2283-2289.

4. S. Goldberger, F. Drummond, J. Barrera, S. Davis, J. Edelen, M. Geppert, Y.-S. Judie, Q. Manley, C. Peters, S. Smith, and G. H. Huff, "Design of a polarization reconfigurable crossed-dipole antenna using surface integrated fluidic loading mechanisms," *2010 URSI Nat. Radio Sci. Meeting*, Boulder, CO, Jan. 2010.

5. S. Goldberger, F. Drummond, R. Anderson, J. Barrera, A. Bolon, S. Davis, J. Edelen, J. Marshall, C. Peters, D. Umana, and G. H. Huff, "Frequency reconfiguration of a small array enabled by functionalized dispersions of colloidal materials," 23rd Annual Conference on Small Satellites, Utah State University, Logan, UT, Aug., 2009.

6. P. Bahukudumbi, W. N. Everett, A. Beskok, M. A. Bevan, G. H. Huff, D. Lagoudas, and Z. Ounaies, "Colloidal microstructures, transport, and impedance properties within interfacial microelectrodes," *Applied Physics Letters,* vol. 90, pp. 224102-224103, 2007.

7. H. Morgan and N. G. Green, *AC Electrokinetics : Colloids and Nanoparticles*. Philadelphia, PA: Research Studies Press, 2003.

8. J. Lee, J. G. Boyd IV, and D. C. Lagoudas, "Effective properties of three-phase electro-magneto-elastic composites," *International Journal of Engineering Science,* vol. 43, pp. 790-825, 2005.

9. A. Sihvola, *Electromagnetic Mixing Formulas and Applications*. London: Institution of Electrical Engineers, 1999.

10. J. A. Stratton, *Electromagnetic Theory*. New York; London: McGraw-Hill book company, inc., 1941.

11. T. B. Jones, *Electromechanics of Particles*. Cambridge, New York: Cambridge University Press, 1995.

12. H. A. Pohl, *Dielectrophoresis: The Behavior of Neutral Matter in Nonuniform Electric Fields*. Cambridge, New York: Cambridge University Press, 1978.

13. C. W. Oatley, *Electric and Magnetic Fields : An Introduction*. Cambridge, New York: Cambridge University Press, 1976.

14. W. E. Langlois, *Slow Viscous Flow*. New York: Macmillan, 1964.

15. N. G. Green, A. Ramos, A. Gonzalez, H. Morgan, and A. Castellanos, "Fluid flow induced by nonuniform ac electric fields in electrolytes on microelectrodes. III. Observation of streamlines and numerical simulation," *Physical Review E,* vol. 66, pp. 026305-026315, 2002.

16. M. Parthasarathy and D. J. Klingenberg, "Electrorheology: Mechanisms and models," *Materials Science and Engineering: R: Reports,* vol. 17, pp. 57-103, 1996.

17. Y. Liu, W. K. Liu, T. Belytschko, N. Patankar, A. C. To, A. Kopacz, and J.-H. Chung, "Immersed electrokinetic finite element method," *International Journal for Numerical Methods in Engineering,* vol. 71, pp. 379-405, 2007.

VITA

Name: Franklin Jerrel Drummond

Address: Department of Electrical and Computer Engineering
                   Texas A&M University
                   214 Zachry Engineering Center,
                   TAMU 3128
                   College Station, TX 77843-3128

Email Address: fjdrummond@gmail.com

Education: B.S., Aerospace Engineering, Texas A&M University
                   College Station, TX, 2008
                   M.S., Aerospace Engineering, Texas A&M University
                   College Station, TX, 2011